



RESEARCH ARTICLE

In vivo Imaging of Cannabinoid Type 2 Receptors: Functional and Structural Alterations in Mouse Model of Cerebral Ischemia by PET and MRI

Ruiqing Ni^{1,2} , Adrienne Müller Herde³, Ahmed Haider³, Claudia Keller³, Georgios Louloudis¹, Markus Vaas¹, Roger Schibli³, Simon M. Ametamey³, Jan Klohs¹, and Linjing Mu^{3,4} 

¹Institute for Biomedical Engineering, University of Zurich & ETH Zurich, Zurich, Switzerland

²Institute for Regenerative Medicine, University of Zurich, Zurich, Switzerland

³Department of Chemistry and Applied Biosciences, ETH Zurich, HCI H427 Vladimir-Prelog-Weg 1-5/10, 8093 Zurich, Switzerland

⁴Department of Nuclear Medicine, University Hospital Zurich, Zurich, Switzerland 2021

Abstract

Purpose: Stroke is one of the most prevalent vascular diseases. Non-invasive molecular imaging methods have the potential to provide critical insights into the temporal dynamics and follow alterations of receptor expression and metabolism in ischemic stroke. The aim of this study was to assess the cannabinoid type 2 receptor (CB₂R) levels in transient middle cerebral artery occlusion (tMCAO) mouse models at subacute stage using positron emission tomography (PET) with our novel tracer [¹⁸F]RoSMA-18-d6 and structural imaging by magnetic resonance imaging (MRI).

Procedures: Our recently developed CB₂R PET tracer [¹⁸F]RoSMA-18-d6 was used for imaging neuroinflammation at 24 h after reperfusion in tMCAO mice. The RNA expression levels of CB₂R and other inflammatory markers were analyzed by quantitative real-time polymerase chain reaction using brain tissues from tMCAO (1 h occlusion) and sham-operated mice. [¹⁸F]fluorodeoxyglucose (FDG) was included for evaluation of the cerebral metabolic rate of glucose (CMRglc). In addition, diffusion-weighted imaging and T₂-weighted imaging were performed for anatomical reference and delineating the lesion in tMCAO mice.

Results: mRNA expressions of inflammatory markers *TNF-α*, *Iba1*, *MMP9* and *GFAP*, *CNR2* were increased to 1.3–2.5 fold at 24 h after reperfusion in the ipsilateral compared to contralateral hemisphere of tMCAO mice, while mRNA expression of the neuronal marker *MAP-2* was markedly reduced to ca. 50%. Reduced [¹⁸F]FDG uptake was observed in the ischemic striatum of tMCAO mouse brain at 24 h after reperfusion. Although higher activity of [¹⁸F]RoSMA-18-d6 in *ex vivo* biodistribution studies and higher standard uptake value ratio (SUVr) were detected in the ischemic ipsilateral compared to contralateral striatum in tMCAO mice, the *in vivo* specificity of [¹⁸F]RoSMA-18-d6 was confirmed only in the CB₂R-rich spleen.

Conclusions: This study revealed an increased [¹⁸F]RoSMA-18-d6 measure of CB₂R and a reduced [¹⁸F]FDG measure of CMRglc in the ischemic striatum of tMCAO mice at subacute stage. [¹⁸F]RoSMA-18-d6 might be a promising PET tracer for detecting CB₂R alterations in animal models of neuroinflammation without neuronal loss.

Key words Cannabinoid type 2 receptor · [¹⁸F]RoSMA-18-d6 · Ischemic stroke · Neuroinflammation · Magnetic resonance imaging · Positron emission tomography

Introduction

The pathophysiology of ischemic stroke is complex and associated with a myriad of cellular and molecular pathways. The severe reduction in cerebral blood flow (CBF) initiates a cascade of hemodynamic, vascular and inflammatory processes in a time-dependent manner in the supplied brain territory, and subsequent defensive response for repair related to lesion expansion and containment. Irreversible tissue damage occurs in the core of the ischemic area, while neurons in the ischemic penumbra face excitotoxicity, peri-infarct polarizations, inflammation, and apoptosis, leading to a secondary tissue damage and expansion of the lesion if reperfusion cannot be restored within an early time frame [1–3]. Neuroinflammation post stroke has been an important therapeutic target. Anti-inflammatory, immunomodulatory treatments and microglia-targeted therapy were evaluated in clinical stroke trials [4–6]. Thus, there is a need for imaging the regional neuroinflammatory pattern for understanding disease mechanism and for therapeutic monitoring.

Positron emission tomography (PET) using [^{18}F]fluorodeoxyglucose ([^{18}F]FDG) for cerebral metabolic rate of glucose (CMRglc), [^{15}O]H $_2$ O for perfusion imaging, and diffusion weighted (DW) magnetic resonance imaging (MRI) are valuable tools to support understanding of the pathophysiology in patients with ischemic stroke [2, 7–13]. However, *in vivo* imaging of neuroinflammation and gliosis is challenging [11, 12, 14]. One reason is that the astrocytes and microglia are highly dynamic and heterogeneous in their subtypes, locations, and activation status [15]. Additionally, the identification of an ideal target for neuroinflammation imaging is highly demanding. Translocator protein (TSPO) is the most widely used neuroinflammation target for PET imaging. [^{11}C]PK-11195, the first-generation TSPO PET tracer, and several second-generation tracers such as [^{11}C]DAA1106, [^{11}C]PBR06, [^{11}C]PBR28, and [^{18}F]DPA-713, [^{18}F]DPA-714, and third-generation tracers [^{11}C]GE180, and [^{11}C]JER176 [16–27], have been evaluated in (pre-)clinical studies. PET imaging studies using TSPO tracers have shown increased brain uptake in post-stroke, although different time course and distribution were detected depending on the animal models and procedures. A faster time-course is observed in permanent compared to temporary ischemic stroke, and a higher increase of TSPO ligand uptake in the infarct core in temporary stroke than in peri-infarct areas in permanent stroke was reported [12, 15, 20, 28]. Thus, the development of novel PET probes for visualizing alternative targets in neuroinflammation have received great attention in recent years [29–32].

Cannabinoid type 2 receptors (CB $_2$ R) are mainly expressed by immune cells including monocytes and macrophages. In the brain, CB $_2$ Rs are primarily found on microglia and have low expression levels under physiological conditions [1, 3, 33]. Upregulation of brain CB $_2$ R expression is reported under acute inflammation such as ischemic stroke, and related to lesion extension in the penumbra and subsequent functional recovery [34]. Treatment with CB $_2$ R agonists has

been shown to be neuroprotective and attenuates macrophage/microglial activation in mouse models of cerebral ischemia [34–38]. CB $_2$ R was also upregulated in other brain diseases with involvement of inflammation/microglia under chronic inflammation in neurodegenerative diseases such as Alzheimer's disease [39–42] and senescence-accelerated models [43] associated with amyloid- β deposits [33, 44–50].

Several structural scaffolds of CB $_2$ R PET tracers have recently been developed [51–55] including pyridine derivatives, oxoquinoline derivatives, thiazole derivatives [56, 57], oxadiazole derivatives [58], carbazole derivatives [59], imidazole derivative [60], and thiophene derivatives [61, 62]. In this study, our newly developed pyridine derivative [^{18}F]RoSMA-18-d6 (Fig. 3b), which exhibited sub-nanomolar affinity and high selectivity towards CB $_2$ R (K $_i$: 0.8 nM, CB $_2$ R/CB $_1$ R > 12'000) [63], was selected for CB $_2$ R-targeted neuroinflammation imaging.

The aim of the current study was to evaluate the novel CB $_2$ R tracer, [^{18}F]RoSMA-18-d6, in the transient middle cerebral artery occlusion (tMCAO) mouse models of focal cerebral ischemia [64–70] using microPET. In addition, [^{18}F]FDG was included for evaluation of the cerebral metabolic rate of glucose (CMRglc) and as a readily available radiotracer benchmark for neuroinflammation [71, 72]. Diffusion-weighted imaging (DWI) and T $_2$ -weighted imaging were performed for anatomical reference and for delineating the lesion in tMCAO mice.

Methods

Radiosynthesis

[^{18}F]RoSMA-18-d6 was synthesized by nucleophilic substitution of the tosylate precursor with [^{18}F]KF/Kryptofix222 in acetonitrile [63]. The crude product was purified by reverse phase semi-preparative high-performance liquid chromatography and formulated with 5 % ethanol in water for intravenous injection and for biological evaluations. In a typical experiment, a moderate radiochemical yield of ~ 12 % (decay corrected) was achieved with a radiochemical purity > 99 %. The molar activities ranged from 156 to 194 GBq/ μmol at the end of synthesis. The identity of the final product was confirmed by comparison with the HPLC retention time of the non-radioactive reference compound by co-injection. [^{18}F]FDG was obtained from a routine clinical production from the University Hospital Zurich, Switzerland.

Animals

Twenty-four male C57BL/6 J mice were obtained from Janvier Labs (Le Genest-Saint-Isle, France). The mice were scanned at 8–10 weeks of age (20–25 g body weight). Mice were randomly allocated to sham-operation ($n = 10$) or tMCAO ($n = 14$). Mice underwent MRI, μPET /computed tomography (CT), and 2,3,5-triphenyltetrazolium chloride

(TTC) histology staining for validation 24 h or 48 h after reperfusion. Animals were housed in ventilated cages inside a temperature-controlled room, under a 12-h dark/light cycle. Pelleted food (3437PXL15, CARGILL) and water were provided ad libitum. Paper tissue and red Tecniplast mouse house® (Tecniplast, Milan, Italy) shelters were placed in cages as environmental enrichments. All experiments were performed in accordance with the Swiss Federal Act on Animal Protection and were approved by the Cantonal Veterinary Office Zurich (permit number: ZH018/14 and ZH264/16).

Surgeries for tMCAO and sham-operation were performed using standard-operating procedures as described before [73, 74]. Anesthesia was initiated by using 3 % isoflurane (Abbott, Cham, Switzerland) in a 1:4 oxygen/air mixture and maintained at 2 %. Before the surgical procedure, a local analgesic (Lidocaine, 0.5 %, 7 mg/kg, Sintectica S.A., Switzerland) was administered subcutaneously (s.c.). Temperature was kept constant at 36.5 ± 0.5 °C with a feedback controlled warming pad system. All surgical procedures were performed in 15–30 min. After surgery, buprenorphine was administered as s.c. injection (Temgesic, 0.1 mg/kg b.w.), and at 4 h after reperfusion and supplied thereafter via drinking water (1 mL/32 mL of drinking water) until 24 h or 48 h. Animals received softened chow in a weighing boat on the cage floor to encourage eating. tMCAO animals were excluded from the study if they met one of the following criteria: Bederson testing was performed 2 h post-reperfusion. Bederson score of 0, no reflow after filament removal, and premature death.

mRNA Isolation, Reverse-Transcription Reaction, and Real-Time Polymerase Chain Reaction

Brain hemispheres of C57BL/6 mouse and tMCAO mice at 24 h and 48 h post reperfusion were used for total mRNA isolation according to the protocols of the Isol-RNA Lysis Reagent (5 PRIME, Gaithersburg, USA) and the bead-milling TissueLyser system (Qiagen, Hilden, Germany). QuantiTect® Reverse Transcription Kit (Qiagen, Hilden, Germany) was used to generate cDNA. The primers (Microsynth, Balgach, Switzerland) used for the quantitative polymerase chain reaction (qPCR) are summarized in Supplementary Table 1. Quantitation of *CNR2*, *ionized calcium binding adaptor molecule 1 (Iba1)*, *tumor necrosis factor (TNF- α)*, *matrix metalloproteinase 9 (MMP9)*, *glial fibrillary acidic protein (GFAP)*, and *microtubule-associated protein 2 (MAP-2)* mRNA expression was performed with the DyNAmo™ Flash SYBR® Green qPCR Kit (Thermo Scientific, Runcorn, UK) using a 7900 HT Fast Real-Time PCR System (Applied Biosystems, Carlsbad, USA). The amplification signals were detected in real-time, which permitted accurate quantification of the amounts of the initial RNA template during 40 cycles according to the manufacturer's protocol. All reactions were performed in duplicates and in two independent runs. Quantitative analysis was performed using the SDS Software (v2.4) and a previously described $2^{-\Delta\Delta Ct}$ quantification

method [75]. The specificity of the PCR products of each run was determined and verified with the SDS dissociation curve analysis feature.

In vivo MRI

Data were acquired at 24 h after reperfusion on a 7 T Bruker Pharmascan (Bruker BioSpin GmbH, Germany), equipped with a volume resonator operating in quadrature mode for excitation and a four-element phased-array surface coil for signal reception and operated by Paravision 6.0 (Bruker BioSpin) [73, 76–78]. Mice were anesthetized with an initial dose of 4 % isoflurane in oxygen/air (200:800 ml/min) and maintained at 1.5 % isoflurane in oxygen/air (100:400 ml/min). Body temperature was monitored with a rectal temperature probe (MLT415, ADInstruments) and kept at 36.5 ± 0.5 °C using a warm water circuit integrated into the animal support (Bruker BioSpin GmbH, Germany). T_2 -weighted MR images were obtained using a spin echo sequence (TurboRARE) with an echo time 3 ms, repetition time 6 ms, 100 averages, slice thickness 1 mm, field-of-view $2.56 \text{ cm} \times 1.28 \text{ cm}$, matrix size 256×128 , giving an in-plane resolution of $100 \mu\text{m} \times 100 \mu\text{m}$. For DWI, a four-shot spin echo–echo planar imaging sequence with an echo time = 28 ms, repetition time = 3000 [76, 77], acquired with a field-of-view of $3.3 \text{ cm} \times 2 \text{ cm}$ and a matrix size of 128×128 , resulting in a nominal voxel size of $258 \mu\text{m} \times 156 \mu\text{m}$. Diffusion-encoding was applied in the x-, y-, and z-directions with b values of 100, 200, 400, 600, 800, and 1000 s/mm^2 , respectively, acquisition time 3 min 48 s. The ischemic lesion was determined as an area of significant reduction of the apparent diffusion coefficient (ADC) value compared with the unaffected contralateral side [79]. On T_2 -weighted images, the lesion was determined as an area of hyperintensities compared with the contralateral side.

In vivo microPET Studies

MicroPET/CT scans were performed at 24 h after reperfusion with a calibrated SuperArgus μ PET/CT scanner (Sedecal, Madrid, Spain) with an axial field-of-view of 4.8 cm and a spatial resolution of 1.6–1.7 mm (full width at half maximum). tMCAO and the sham-operated C57BL/6 J mice were anesthetized with ca. 2.5 % isoflurane in oxygen/air (1:1) during tracer injection and the whole scan time period. The formulated radioligand solution ($[^{18}\text{F}]\text{FDG}$: 9.9–11 MBq or $[^{18}\text{F}]\text{RoSMA-18-d6}$: 7.2–13 MBq) was administered via tail vein injection, and mice were dynamically scanned for 60 min. For blocking experiments, 1.5 mg/kg GW405833 (Fig. 3a) was dissolved in a vehicle of 2 % Cremophor (v/v), 10 % ethanol (v/v), and 88 % water for injection (v/v) and injected together with $[^{18}\text{F}]\text{RoSMA-18-d6}$. Body temperature was monitored by a rectal probe and kept at 37 °C by a heated air stream (37 °C). The anesthesia depth was measured

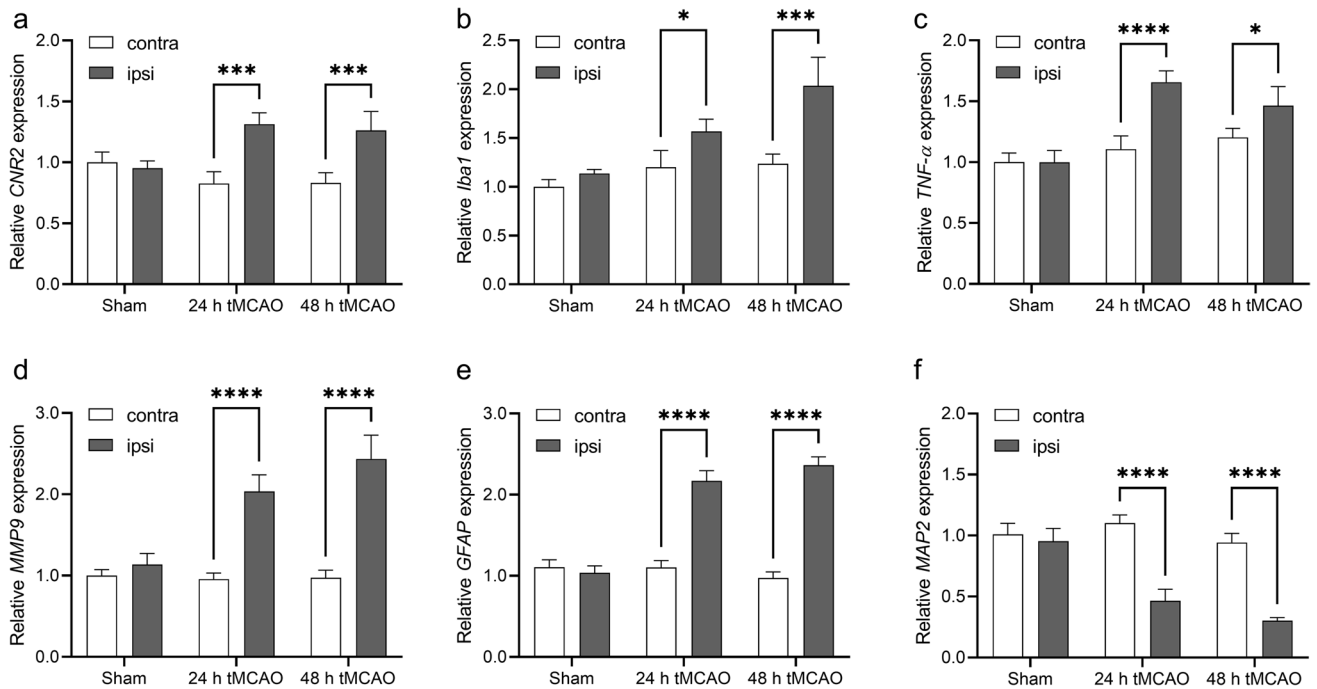


Fig. 1. Relative mRNA levels of inflammatory markers and neuronal damage in sham-operated and tMCAO mouse brain in contra- and ipsilateral brain hemisphere at 24 h and 48 h after reperfusion. **a** *CNR2*, **b** *Iba1*, **c** *TNF-α*, **d** *MMP9*, **e** *GFAP*, and **f** *MAP2*. Values represent mean \pm standard deviation. Expression levels were quantified by qPCR relative to β -actin. * $p < 0.05$, *** $p < 0.001$, **** $p < 0.0001$.

by the respiratory frequency (SA Instruments, Inc., Stony Brook, USA). μ PET acquisitions were combined with CT for anatomical orientation and attenuation correction. The obtained data were reconstructed in user-defined time frames with a voxel size of $0.3875 \times 0.3875 \times 0.775 \text{ mm}^3$ as previously described [80].

Triphenyltetrazolium Chloride (TTC) Staining

To assess the ischemic lesion severity in the brain of tMCAO mice and to validate the absence of lesion in the sham-operated mice, staining with TTC staining was performed. After measurements mice were euthanized, their brains were removed and 1-mm thick brain slices were obtained with a brain matrix. Slices were incubated in a 2.5% TTC solution (Sigma-Aldrich, Switzerland) in PBS at 37 °C for 3 min. Photographs of the brain sections were taken. Edema-corrected lesion volumes were quantified as described [81].

Biodistribution Studies in the Mouse Brain

After PET/CT scanning of tMCAO mice at 24 h after reperfusion with [^{18}F]RoSMA-18-d6, animals were sacrificed at 70 min post injection by decapitation. The spleen and brain regions of ischemic ipsilateral area and contralateral hemisphere were collected for analysis with a gamma counter. The accumulated radioactivities in the different tissues were expressed as percent normalized injected dose per gram of tissue normalized to 20 g body weight of the animals (norm. percentage injected dose per gram tissue (% ID/g tissue)).

Data Analysis and Statistics

Images were processed and analyzed using PMOD 4.2 software (PMOD Technologies Ltd., Zurich, Switzerland). The time–activity curves were deduced from specific volume-of-interest that were defined based on a mouse MRI T_2 -weighted image template [82]. Radioactivity is presented as standardized uptake value (SUV) (decay-corrected radioactivity per cm^3 divided by the injected dose per gram body weight). [^{18}F]RoSMA-18-d6 SUV was calculated by using the midbrain in the corresponding hemisphere as reference brain region. For [^{18}F]FDG PET, regional SUV was calculated. Two-way ANOVA with Sidak post hoc analysis was used for comparison between groups (Graphpad Prism 9.0, CA, USA).

Results

Increased expression of inflammation makers and neuronal damage after focal cerebral ischemia in tMCAO mice mRNA levels were measured to address the question whether mouse non-ischemic and ischemic hemispheres differ in their expression levels of *CNR2* and other inflammatory genes. *CNR2* mRNA expression was increased to around 1.3-fold after 24 h reperfusion and at 48 h in the ipsilateral comparing to contralateral hemisphere (Fig. 1a). Similarly, 1.5–2.5-fold increases were observed in the mRNA expression of inflammatory markers including *TNF-α*, *Iba1*, *MMP9*, and *GFAP* at 24 h and 48 h after reperfusion in the ipsilateral compared to contralateral brain region (Fig. 1b–e). *MAP2*

expression has been shown to be a reliable marker of neurons that undergo cell death [83, 84]. The neuron-specific *MAP-2* expression was markedly reduced in the ipsilateral compared to contralateral hemisphere at 24 h and 48 h after reperfusion (Fig. 1f). As similar *CNR2* mRNA expression was observed at 24 h and 48 h, our studies were performed at early time point of 24 h after reperfusion for investigating the functional, structural, and molecular changes in the following experiments.

Reduced Cerebral Glucose Metabolism and Structural MRI Lesion Following tMCAO

Reduced [^{18}F]FDG uptake was observed in the presumed MCA territory of the ipsilateral hemisphere in tMCAO mice, while there was no difference in [^{18}F]FDG uptake between hemispheres in sham-operated mice (Fig. 2a). SUVs were significantly lower in the ipsilateral striatum in tMCAO compared to the contralateral side and compared to the same region in sham-operated mice 1.8 vs 1.4 (Fig. 2b). There were no differences in [^{18}F]FDG uptake in the cortex and cerebellum between the ipsilateral and contralateral hemisphere in tMCAO mice and sham-operated mice. T_2 -weighted MRI and

DWI imaging were performed in tMCAO and sham-operated animals at 24 h after reperfusion (Fig. 2c). The lesions in the ipsilateral side in the striatum and cortex were visible as areas of decreased values on the ADC maps calculated from DWI and as areas of increased intensities on the T_2 -weighted MR images at 24 h after reperfusion following 1 h tMCAO (Figs. 2c–d). Ischemic lesions in the tMCAO were also seen *ex vivo* as white areas, while viable tissue appeared red in TTC stained brain sections (Fig. 2e). Homogenous deep red color was observed across both hemispheres in sham-operated mice, verifying the absence of any lesion. The hemispheric lesion volumes in tMCAO mice were $42.8 \pm 10.2\%$ (mean \pm standard deviation).

Increased [^{18}F]RoSMA-18-d6 Retention in the Striatum After tMCAO

To analyze the distribution of [^{18}F]RoSMA-18-d6 in tMCAO mice brain, dynamic $\mu\text{PET}/\text{CT}$ scans were performed at 24 h after reperfusion. The standard uptake values (SUVs) of [^{18}F]RoSMA-18-d6 did not reveal significant difference in various brain regions of tMCAO mice (Supplementary Fig. 1). However, we found a reduced uptake at early time frame

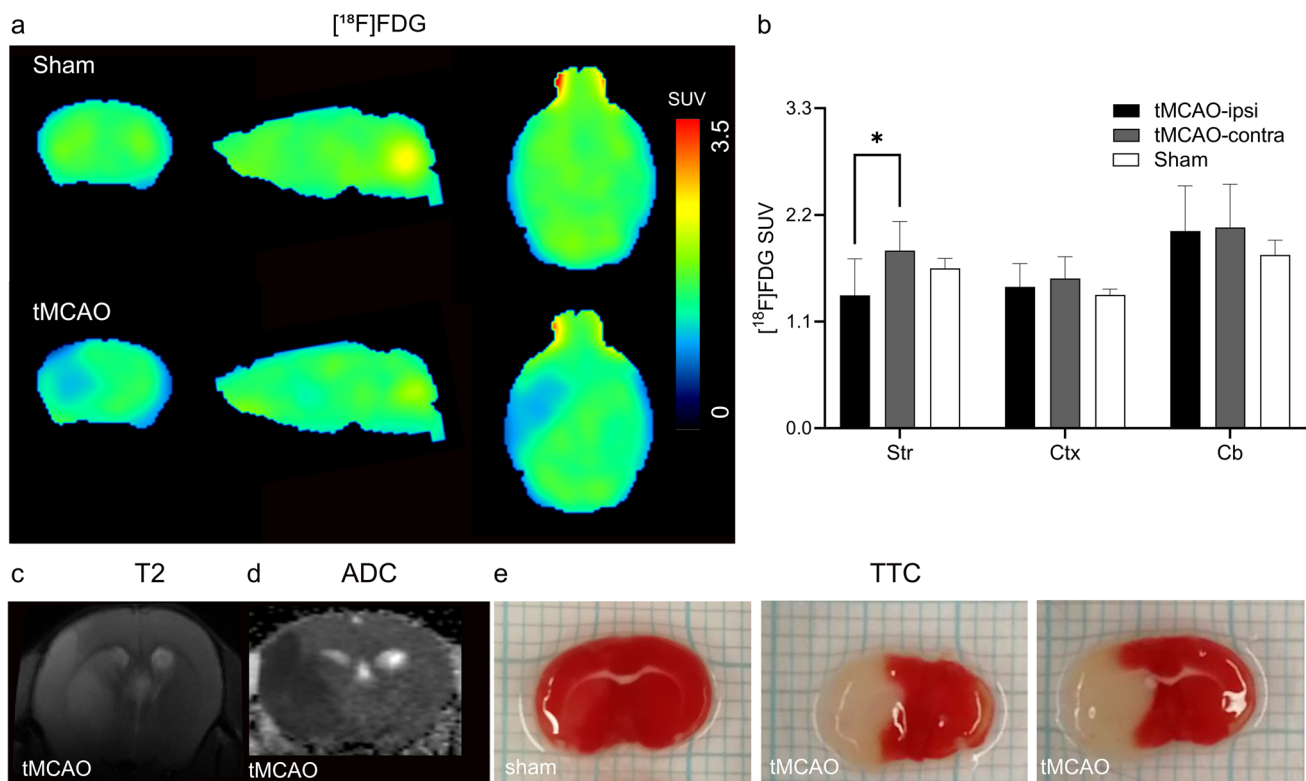
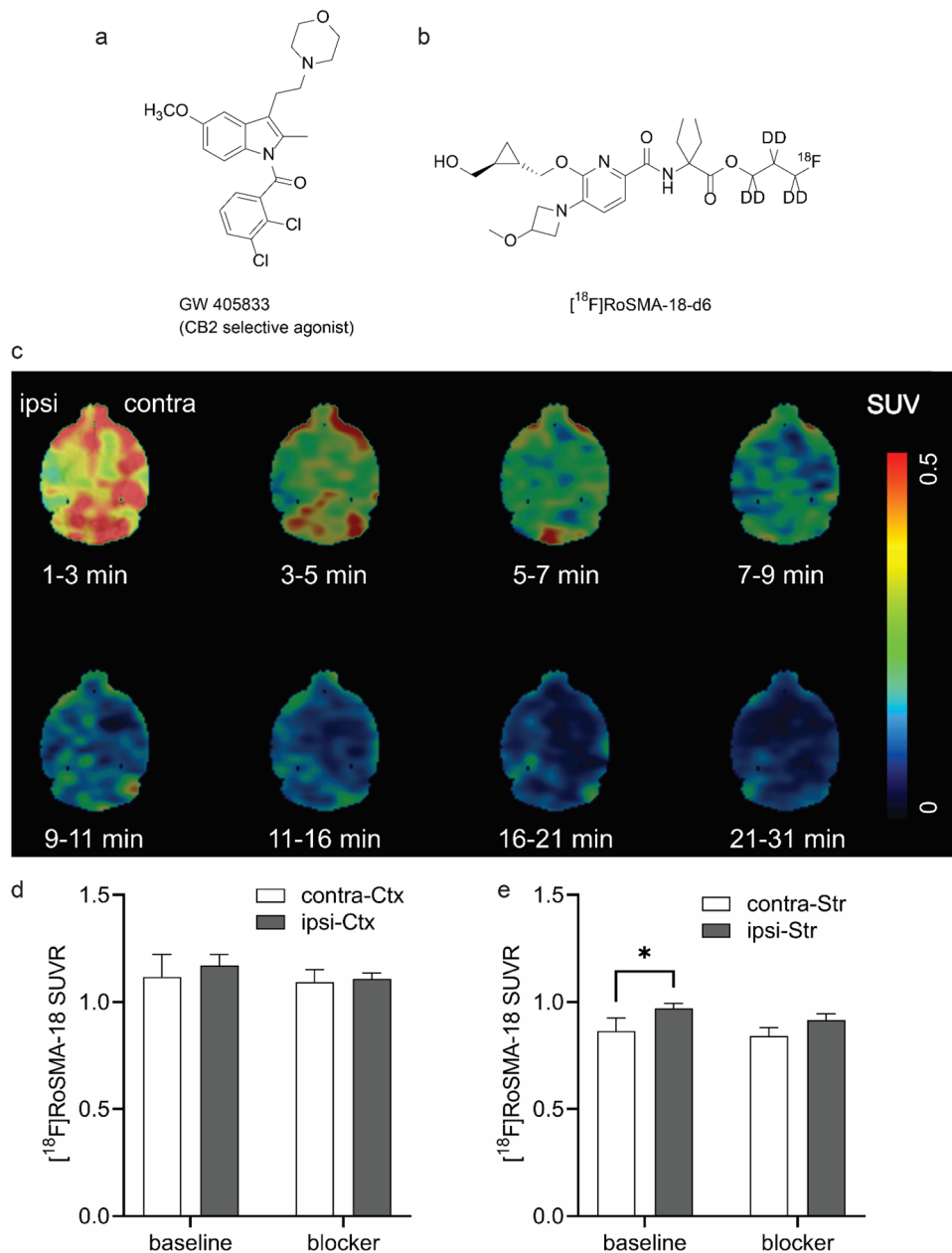


Fig. 2. *In vivo* MRI and [^{18}F]FDG PET in tMCAO mouse brain. **a** Representative PET images of coronal, sagittal and horizontal mouse brain sections after intravenous injection of [^{18}F]FDG in sham-operated and tMCAO mice. The radiosignals were averaged from 21 to 61 min; **b** [^{18}F]FDG accumulation (SUV) at different mouse brain regions (Str: striatum; Ctx: cortex; Cb: cerebellum) in sham and tMCAO mice. Significantly reduced [^{18}F]FDG accumulation was observed in the ipsilateral striatum compared to contralateral side in tMCAO mice; **c–e** *in vivo* T_2 -weighted image, ADC map, and *ex vivo* TTC stained brain sections, indicating the delineation in tMCAO mice. TTC, 2,3,5-triphenyltetrazolium chloride; ADC, apparent diffusion coefficient; SUV, standard uptake value. * $p < 0.05$.

Fig. 3. *In vivo* microPET imaging of tMCAO mouse brain using [^{18}F]RoSMA-18-d6.

a,b Chemical structures of blocker GW405833 and [^{18}F]RoSMA-18-d6; **c** representative PET images of horizontal mouse brain sections at different time frames after intravenous injection of [^{18}F]RoSMA-18-d6; SUV: 0–0.5; **d,e** ratios of [^{18}F]RoSMA-18-d6 uptake under baseline and blockade conditions in cortex and striatum. Significantly higher [^{18}F]RoSMA-18-d6 standard uptake value ratio (SUVR) was observed in the ischemic ipsilateral striatum under baseline conditions, but not in the ipsilateral cortex. Midbrain was used as reference brain region for SUVR calculation. * $p < 0.05$.



(1–3 min) and a similar uptake after 7 min in the ipsilateral side compared to that of the contralateral side (Fig. 3c, and whole head images in Supplementary Fig. 2). Thus, to exclude the perfusion influence, we averaged the brain signals from 21–61 min and selected the midbrain as the reference region. Higher [^{18}F]RoSMA-18-d6 SUVR was observed in the ischemic ipsilateral striatum compared to the contralateral striatum (two-way ANOVA with Sidak multiple comparison correction, 0.97 ± 0.02 vs 0.87 ± 0.06 , $p = 0.0274$), but not in other brain regions such as cortex (Figs. 3d, e). The increased signals at ischemic ipsilateral striatum, however, could not be blocked by the selective CB₂R agonist GW405833 (Fig. 3e).

At the end of the *in vivo* experiments, we dissected the mice to verify the activity accumulation and specificity

of [^{18}F]RoSMA-18-d6 in the spleen and different brain regions with a gamma counter. In line with the results obtained from the averaged SUVRs in the tMCAO mouse brain, the radioactivity in the ipsilateral side was indeed significantly higher than that of the contralateral hemisphere (0.037 ± 0.007 vs 0.026 ± 0.003 , $n = 5$ each group), but no blockade effect was seen under blocking conditions (Fig. 4a). As expected, radioactivity in the CB₂R-rich spleen was much higher than the brain and 58% of the signals was blocked by co-injection of CB₂R specific ligand GW405833, demonstrating specific target engagement of [^{18}F]RoSMA-18-d6 *in vivo* (Fig. 4b).

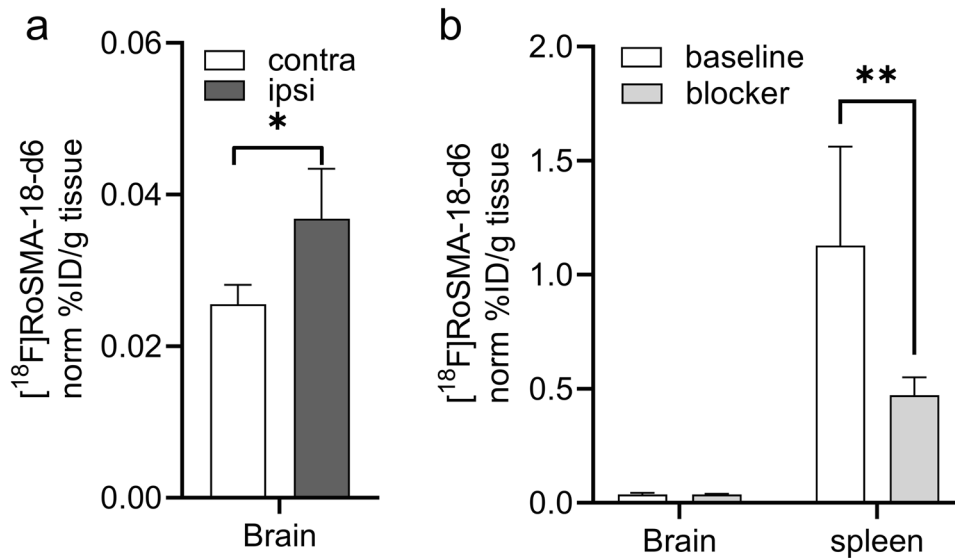


Fig. 4. *Ex vivo* biodistribution of $[^{18}\text{F}]$ RoSMA-18-d6 in the brain and spleen of tMCAO mouse. Animals ($n=4$) were sacrificed at 70 min post-injection, and the spleen and brain regions were dissected and analyzed with a gamma counter. **a** Higher $[^{18}\text{F}]$ RoSMA-18-d6 binding (norm % ID/g tissue) was detected in the ipsilateral vs contralateral hemisphere under baseline conditions. **b** In the spleen about 58% of the $[^{18}\text{F}]$ RoSMA-18-d6 binding (norm % ID/g tissue) was blocked. No significant blocking was observed in the brain. Data are presented as the mean of the percentage of injected dose per gram tissue normalized to 20 g body weight; mean \pm standard deviation. % ID/g: percentage injected dose per gram. * $p < 0.05$, ** $p < 0.01$.

Discussion

This study assessed the utility of CB_2R PET tracer $[^{18}\text{F}]$ RoSMA-18-d6 for imaging tMCAO mouse at subacute stage, concomitant with decreased CMRglc levels and formation of a structural lesion. Previous PET imaging of stroke animal models led to inconclusive results. In a rat model of photothrombotic stroke at 24 h after surgery, increased $[^{11}\text{C}]$ NE40 (CB_2R tracer) uptake and unvaried $[^{11}\text{C}]$ PK11195 (TSPO tracer) uptake were reported [85]. In another study, $[^{11}\text{C}]$ NE40 uptake did not show any difference in the same rat model of photothrombotic stroke [86]. Moreover, reduced $[^{11}\text{C}]$ A836339 (CB_2R tracer) uptake was reported in a focal tMCAO rat model over 1–28 days after occlusion [56]. Possible reasons for these different observations include the time point of assessment, different methods for inducing acute stroke (transient or permanent ischemia) resulting in variations of ischemic severity and levels of inflammatory cell expression [36].

CB_2R has negligible expression in the mouse brain and is mainly expressed in the spleen under physiological conditions [39, 45, 64–69, 87]. Under neuroinflammatory conditions, CB_2R is upregulated in activated microglial cells. In this study, we used quantitative real-time polymerase chain reaction to measure gene expression levels of *CNR2*, *TNF- α* , *Ibal*, *MMP9*, *GFAP*, and *MAP-2* at 24 h and 48 h. All tested inflammatory markers displayed increased mRNA levels in the ipsilateral brain hemisphere, in agreement with the reported findings in tMCAO mouse model [34, 38, 88, 89]. In line with the increased *CNR2* gene expression levels, significantly higher $[^{18}\text{F}]$ RoSMA-18-d6 SUVR (standard

uptake value ratio) was observed in striatum at ipsilateral vs contralateral under baseline conditions in our PET studies. The 50% reduction of the neuronal marker *MAP-2* indicated neuronal damage.

The dynamic μPET scan using $[^{18}\text{F}]$ RoSMA-18-d6 indicated a reduced perfusion in the lesion brain regions at the first time frame of 1–3 min. This is probably due to the changes of microvascular response (no-reflow phenomenon) and the reduction in neuronal activity. Taking the midbrain as the reference region, the ratios of SUV averaged from 21 to 61 min revealed increased $[^{18}\text{F}]$ RoSMA-18-d6 SUVR in the ipsilateral ischemic striatum compared to that of the contralateral side. Our *ex vivo* bio-distribution studies confirmed the difference of the radioactivity distribution in the left and right brain hemisphere. The *in vivo* specificity of $[^{18}\text{F}]$ RoSMA-18-d6 towards CB_2R is evidenced by a 58% reduction in radioactivity in the mouse spleen under blockade conditions in *ex vivo* bio-distribution studies. Underlying reasons for the lack of specificity of $[^{18}\text{F}]$ RoSMA-18-d6 in the mouse brain may include (1) the increased tracer availability in the blood induced by blocking the CB_2R peripheral targets in the presence of the blocker GW405833; and (2) the relatively low brain uptake of our CB_2R -selective radioligand $[^{18}\text{F}]$ RoSMA-18-d6 in the mouse brain resulted in undetectable changes of radiosignals under baseline and blockade conditions. Notably, the time-activity curves of $[^{18}\text{F}]$ RoSMA-18-d6 in tMCAO mouse brain showed remarkably higher initial brain uptake under blockade conditions than the baseline in both sides of the mouse brain (Supplementary Fig. 1), indicating the influence of blocking CB_2R target

in the peripheral organs on the availability of radiotracer concentrations in the blood. In our previous studies with Wistar rats, the spleen uptake of [^{18}F]RoSMA-18-d6 was blocked by nearly 90%. The higher specific binding of [^{18}F]RoSMA-18-d6 in rat spleen is likely due to the increased available targets. Govaerts et al. reported higher binding sites B_{max} in the rat spleen (0.71 ± 0.02 pmol/mg protein) compared to that in the mouse spleen (0.31 ± 0.03 pmol/mg protein) by using [^3H]CP55940 binding assay [90]. In the mouse P-glycoprotein assay, compound RoSMA-18 exhibits an efflux ratio (ER) of 4.6, which partly explains the low initial brain uptake in mice. Compared to other CB_2R radioligand developed in our group, [^{18}F]ROSMA-18-d6 has the highest specificity (86%) towards CB_2R based on the *ex vivo* biodistribution results in the rat spleen and was therefore selected for *in vivo* studies.

We observed that [^{18}F]FDG measure of CMR_{glc} was reduced in the ischemic areas, i.e., ipsilateral striatum of the tMCAO mice at 24 h after reperfusion. The reduced CMR_{glc} was reported in many earlier studies in disease animal models and in stroke patients, [91–94], masking CMR_{glc} reduction of neuronal tissue in the brain. At an extended time points of the recovery stage from days 4 to 40, an increased CMR_{glc} level was reported in the ischemic regions due to the increased consumption from inflammatory cells along with microglial activation [91, 95, 96].

There are several limitations in the current study. (1) As there is no reliable specific CB_2R antibody, we did not include immunohistochemical staining for CB_2R protein distribution in the mouse brain. The qPCR measures of *CNR2* mRNA level provided an alternative readout, but do not provide spatial distribution of cerebral CB_2R expression. (2) Due to the logistic barrier, MRI and $\mu\text{PET}/\text{CT}$ scans were performed with different cohorts of animals. Nevertheless, standard operating procedures for the surgery were used. (3) Our *in vivo* data with tMCAO mice were collected at 24 h after surgery, longitudinal imaging of tMCAO mice with [^{18}F]RoSMA-18-d6 along with structural and functional readout will provide further insight into the spatio-temporal dynamics of CB_2R expression in the brain. Moreover, [^{18}F]FDG-PET was used as a benchmark for neuroinflammation in the current study. Further study using TSPO tracer to assess the glial activation along with CB_2R tracer will provide valuable insights.

Conclusion

Our newly developed CB_2R PET tracer, [^{18}F]RoSMA-18-d6, revealed limited utility to image neuroinflammation in the ischemic ipsilateral of the tMCAO mice at 24 h after reperfusion. Although lesion regions in tMCAO mouse brain could be followed by the ratios of averaged SUVs from 21 to 61 min

with midbrain as the reference region, the *in vivo* specificity of [^{18}F]RoSMA-18-d6 was confirmed only in the CB_2R -rich spleen. Different neuroinflammatory animal models which have comparable neuronal numbers in the lesion regions are recommended for evaluation of CB_2R in further PET imaging studies.

Supplementary Information The online version contains supplementary material available at <https://doi.org/10.1007/s11307-021-01655-4>.

Acknowledgements The authors acknowledge Yingfang He and Annette Krämer at Center for Radiopharmaceutical Sciences, Department of Chemistry and Applied Biosciences, ETH Zurich, and Dr Mark Augath, at the Institute for Biomedical Engineering, ETH Zurich, and University of Zurich, for technical assistance.

Author Contributions RN, JK, LM, and SMA designed the study; RN, KC, AH, AMH, GL, and LM performed the experiment; RN and LM performed data analysis; RN, JK, and LM wrote the initial manuscript. All authors read and approved the final manuscript.

Funding Open access funding provided by Swiss Federal Institute of Technology Zurich. JK received funding from the Swiss National Science Foundation (320030_179277), in the framework of ERA-NET NEURON (32NE30_173678/1), the Synapsis Foundation, the Olga Mayenfisch Stiftung, and the Vontobel foundation. RN received funding from Forschungskredit, Synapsis foundation career development award (2017 CDA-03), and the Vontobel foundation.

Declarations

Conflict of interest The authors declare that they have no conflicts of interest.

Open Access This article is licensed under a Creative Commons Attribution 4.0 International License, which permits use, sharing, adaptation, distribution and reproduction in any medium or format, as long as you give appropriate credit to the original author(s) and the source, provide a link to the Creative Commons licence, and indicate if changes were made. The images or other third party material in this article are included in the article's Creative Commons licence, unless indicated otherwise in a credit line to the material. If material is not included in the article's Creative Commons licence and your intended use is not permitted by statutory regulation or exceeds the permitted use, you will need to obtain permission directly from the copyright holder. To view a copy of this licence, visit <http://creativecommons.org/licenses/by/4.0/>.

References

1. Astrup J (1982) Energy-requiring cell functions in the ischemic brain. Their critical supply and possible inhibition in protective therapy. *J Neurosurg* 56:482–497
2. Heiss W-D (2000) Ischemic penumbra: evidence from functional imaging in man. *J Cereb Blood Flow Metab* 20:1276–1293
3. Dirnagl U, Iadecola C, Moskowitz MA (1999) Pathobiology of ischemic stroke: an integrated view. *Trends Neurosci* 22:391–397
4. Dabrowska S, Andrzejewska A, Lukomska B, Janowski M (2019) Neuroinflammation as a target for treatment of stroke using mesenchymal stem cells and extracellular vesicles. *J Neuroinflamm* 16:178
5. Anrather J, Iadecola C (2016) Inflammation and stroke: an overview. *Neurotherapeutics* 13:661–670
6. Lambertsen KL, Finsen B, Clausen BH (2019) Post-stroke inflammation—target or tool for therapy? *Acta Neuropathol* 137:693–714
7. Evans NR et al (2017) PET imaging of the neurovascular interface in cerebrovascular disease. *Nat Rev Neurol* 13:676–688

8. Marchal G et al (1993) PET imaging of cerebral perfusion and oxygen consumption in acute ischaemic stroke: relation to outcome. *Lancet* 341:925–927
9. Muir KW, Buchan A, von Kummer R, Rother J, Baron J-C (2006) Imaging of acute stroke. *Lancet Neurol* 5:755–768
10. Carter SF et al (2019) Astrocyte biomarkers in Alzheimer's disease. *Trends Mol Med* 25:77–95
11. Jain P et al (2020) Neuroinflammation PET imaging: current opinion and future directions. *J Nucl Med* 61:1107–1112
12. Zinnhardt B et al (2018) In vivo imaging biomarkers of neuroinflammation in the development and assessment of stroke therapies - towards clinical translation. *Theranostics* 8:2603–2620
13. Martín A et al (2012) Imaging of perfusion, angiogenesis, and tissue elasticity after stroke. *J Cereb Blood Flow Metab* 32:1496–1507
14. Venneti S, Lopresti BJ, Wiley CA (2013) Molecular imaging of microglia/macrophages in the brain. *Glia* 61:10–23
15. Kreisler WC et al (2020) PET imaging of neuroinflammation in neurological disorders. *The Lancet Neurology* 19:940–950
16. Thiel A, Heiss WD (2011) Imaging of microglia activation in stroke. *Stroke* 42:507–512
17. Boutin H et al (2015) 18F-GE-180: a novel TSPO radiotracer compared to 11C-R-PK11195 in a preclinical model of stroke. *Eur J Nucl Med Mol Imag* 42:503–511
18. Lartey FM et al (2014) PET Imaging of stroke-induced neuroinflammation in mice using [18F]PBR06. *Mol Imag Biol* 16:109–117
19. Tóth M et al (2016) Acute neuroinflammation in a clinically relevant focal cortical ischemic stroke model in rat: longitudinal positron emission tomography and immunofluorescent tracking. *Brain Struct Funct* 221:1279–1290
20. Chaney A, et al (2018) 11C-DPA-713 versus 18F-GE-180: a preclinical comparison of TSPO-PET tracers to visualize acute and chronic neuroinflammation in a mouse model of ischemic stroke. *J Nucl Med*
21. Martín A et al (2009) Evaluation of the PBR/TSPO radioligand [18F]DPA-714 in a rat model of focal cerebral ischemia. *J Cereb Blood Flow Metab* 30:230–241
22. Thiel A et al (2010) The temporal dynamics of poststroke neuroinflammation: a longitudinal diffusion tensor imaging-guided pet study with ¹¹C-PK11195 in acute subcortical stroke. *J Nucl Med* 51:1404–1412
23. Zinnhardt B et al (2015) Multimodal imaging reveals temporal and spatial microglia and matrix metalloproteinase activity after experimental stroke. *J Cereb Blood Flow Metab* 35:1711–1721
24. Ishikawa A et al (2018) In vivo visualization of Tau accumulation, microglial activation, and brain atrophy in a mouse model of tauopathy rTg4510. *J Alzheimer's Dis* 61:1037–1052
25. Zhou R et al (2021) PET imaging of neuroinflammation in Alzheimer's disease. *Front Immunol* 12:739130
26. Zanotti-Fregonara P et al (2019) Head-to-head comparison of (11)C-PBR28 and (11)C-ER176 for quantification of the translocator protein in the human brain. *Eur J Nucl Med Mol Imaging* 46:1822–1829
27. Ni R et al (2021) In vitro characterization of the regional binding distribution of amyloid PET tracer florbetaben and the glia tracers deprenyl and PK11195 in autopsy Alzheimer's brain tissue. *J Alzheimers Dis* 80:1723–1737
28. Boutin H, Pinborg LH (2015) TSPO imaging in stroke: from animal models to human subjects. *Clin Transl Imaging* 3:423–435
29. Razansky D, Klohs J, Ni R (2021) Multi-scale optoacoustic molecular imaging of brain diseases. *Eur J Nucl Med Mol Imaging*
30. Ling X et al (2015) A novel near-infrared fluorescence imaging probe that preferentially binds to cannabinoid receptors CB2R over CB1R. *Biomaterials* 57:169–178
31. Sarott RC et al (2020) Development of high-specificity fluorescent probes to enable cannabinoid type 2 receptor studies in living cells. *J Am Chem Soc* 142:16953–16964
32. Shi X-F et al (2021) Multimodal contrast agents for optoacoustic brain imaging in small animals. *Front Bioeng Biotechnol* 9:746815
33. Stempel AV et al (2016) Cannabinoid type 2 receptors mediate a cell type-specific plasticity in the hippocampus. *Neuron* 90:795–809
34. Zarruk JG et al (2012) Cannabinoid type 2 receptor activation downregulates stroke-induced classic and alternative brain macrophage/microglial activation concomitant to neuroprotection. *Stroke* 43:211–219
35. Ronca RD et al (2015) A selective cannabinoid CB2 agonist attenuates damage and improves memory retention following stroke in mice. *Life Sci* 138:72–77
36. Bravo-Ferrer I et al (2017) Cannabinoid type-2 receptor drives neurogenesis and improves functional outcome after stroke. *Stroke* 48:204–212
37. Zhang M et al (2007) Cannabinoid CB(2) receptor activation decreases cerebral infarction in a mouse focal ischemia/reperfusion model. *J Cereb Blood Flow Metab* 27:1387–1396
38. Yu SJ, et al (2015) Time-dependent protection of CB2 receptor agonist in stroke. *PLoS ONE* 10:e0132487
39. López A et al (2018) Cannabinoid CB2 receptors in the mouse brain: relevance for Alzheimer's disease. *J Neuroinflamm* 15:158
40. Rodríguez-Vieitez E et al (2015) Astrocytosis precedes amyloid plaque deposition in Alzheimer APPswe transgenic mouse brain: a correlative positron emission tomography and in vitro imaging study. *Eur J Nucl Med Mol Imaging* 42:1119–1132
41. Heneka MT et al (2015) Neuroinflammation in Alzheimer's disease. *Lancet Neurol* 14:388–405
42. Rapic S et al (2013) Imaging microglial activation and glucose consumption in a mouse model of Alzheimer's disease. *Neurobiol Aging* 34:351–354
43. Yamagishi S et al (2019) Upregulation of cannabinoid receptor type 2, but not TSPO, in senescence-accelerated neuroinflammation in mice: a positron emission tomography study. *J Neuroinflamm* 16:208
44. Di Marzo V, Stella N, Zimmer A (2015) Endocannabinoid signalling and the deteriorating brain. *Nat Rev Neurosci* 16:30–42
45. Van Sickle MD et al (2005) Identification and functional characterization of brainstem cannabinoid CB2 receptors. *Science* 310:329–332
46. Xi ZX et al (2011) Brain cannabinoid CB(2) receptors modulate cocaine's actions in mice. *Nat Neurosci* 14:1160–1166
47. Benito C, Tolón RM, Pazos MR (2008) Cannabinoid CB2 receptors in human brain inflammation. *Br J Pharmacol* 153
48. Koppel J, et al (2014) CB2 receptor deficiency increases amyloid pathology and alters Tau processing in a transgenic mouse model of Alzheimer's disease. 20
49. Aso E, Ferrer I (2016) CB2 cannabinoid receptor as potential target against Alzheimer's disease. *Front Neurosci* 10
50. Parbo P et al (2017) Brain inflammation accompanies amyloid in the majority of mild cognitive impairment cases due to Alzheimer's disease. *Brain* 140:2002–2011
51. Spinelli F, Capparelli E, Abate C, Colabufo NA, Contino M (2017) Perspectives of cannabinoid type 2 receptor (CB2R) ligands in neurodegenerative disorders: structure-affinity relationship (SAfIR) and structure-activity relationship (SAR) studies. *J Med Chem*
52. Ni R, Mu L, Ametamey S (2019) Positron emission tomography of type 2 cannabinoid receptors for detecting inflammation in the central nervous system. *Acta Pharmacol Sin* 40:351–357
53. Spinelli F, Mu L, Ametamey SM (2018) Radioligands for positron emission tomography imaging of cannabinoid type 2 receptor. *J Labelled Comp Radiopharm* 61:299–308
54. Hou L et al (2021) Positron emission tomography imaging of the endocannabinoid system: opportunities and challenges in radiotracer development. *J Med Chem* 64:123–149
55. Varlow C, Boileau I, Wey HY, Liang SH, Vasdev N (2020) Classics in neuroimaging: imaging the endocannabinoid pathway with PET. *ACS Chem Neurosci* 11:1855–1862
56. Pottier G et al (2017) PET imaging of cannabinoid type 2 receptors with [11C]JA-836339 did not evidence changes following neuroinflammation in rats. *J Cereb Blood Flow Metab* 37:1163–1178
57. Moldovan R-P et al (2015) 18F-JHU94620, a high affinity PET radioligand for imaging of cannabinoid subtype 2 receptors (CB2R). *J Nucl Med* 56:1048–1048
58. Attili B et al (2019) Preclinical evaluation of [(18)F]MA3: a CB2 receptor agonist radiotracer for PET. *Br J Pharmacol* 176:1481–1491
59. Heimann D et al (2018) Optimization of pharmacokinetic properties by modification of a carbazole-based cannabinoid receptor subtype 2 (CB(2)) ligand. *Eur J Med Chem* 143:1436–1447
60. Kallinen A et al (2019) Synthesis and in vitro evaluation of fluorine-18 benzimidazole sulfones as CB2 PET-radioligands. *Org Biomol Chem* 17:5086–5098
61. Haider A et al (2016) Synthesis and biological evaluation of thiophene-based cannabinoid receptor type 2 radiotracers for PET imaging. *Front Neurosci* 10:350
62. Caillé F et al (2017) Biodistribution of [18F] FC0324, a new PET tracer targeting CB2 receptors. *J Nucl Med* 58:855–855

63. Haider A et al (2020) Identification and preclinical development of a 2,5,6-trisubstituted fluorinated pyridine derivative as a radioligand for the positron emission tomography imaging of cannabinoid type 2 receptors. *J Med Chem* 63:10287–10306
64. Offner H et al (2006) Experimental stroke induces massive, rapid activation of the peripheral immune system. *J Cereb Blood Flow Metab* 26:654–665
65. Garbuzova-Davis S et al (2016) Blood-spinal cord barrier alterations in subacute and chronic stages of a rat model of focal cerebral ischemia. *J Neuropathol Exp Neurol* 75:673–688
66. Huang B et al (2016) GlyT1 Inhibitor NFPS Exerts Neuroprotection via GlyR alpha1 subunit in the rat Model of transient focal cerebral ischaemia and reperfusion. *Cell Physiol Biochem* 38:1952–1962
67. Dang G et al (2016) Dynamic secondary degeneration in the spinal cord and ventral root after a focal cerebral infarction among hypertensive rats. *Sci Rep* 6:22655
68. Moisse K, Welch I, Hill T, Volkening K, Strong MJ (2008) Transient middle cerebral artery occlusion induces microglial priming in the lumbar spinal cord: a novel model of neuroinflammation. *J Neuroinflamm* 5:29
69. Dang G et al (2018) Alterations in the spinal cord and ventral root after cerebral infarction in non-human primates. *Restor Neurol Neurosci* 36:729–740
70. Saleh A et al (2004) In vivo MRI of brain inflammation in human ischaemic stroke. *Brain* 127:1670–1677
71. Love C, Tomas MB, Tronco GG, Palestro CJ (2005) FDG PET of infection and inflammation. *Radiographics* 25:1357–1368
72. Probasco JC, et al (2017) Abnormal brain metabolism on FDG-PET/CT is a common early finding in autoimmune encephalitis. *Neurology(R)* 4:e352
73. Ni R, Vaas M, Ren W, Klohs J (2018) Non-invasive detection of acute cerebral hypoxia and subsequent matrix-metalloproteinase activity in a mouse model of cerebral ischemia using multispectral-optoacoustic-tomography. *Neurophotonics* 5:015005
74. Vaas M, Ni R, Rudin M, Kipar A, Klohs J (2017) Extracerebral tissue damage in the intraluminal filament mouse model of middle cerebral artery occlusion. *Front Neurol* 8:85
75. Livak KJ, Schmittgen TD (2001) Analysis of relative gene expression data using real-time quantitative PCR and the $2^{-\Delta\Delta C(T)}$ method. *Methods* 25:402–408
76. Ni R et al (2019) fMRI reveals mitigation of cerebrovascular dysfunction by bradykinin receptors 1 and 2 inhibitor noscapine in a mouse model of cerebral amyloidosis. *Front Aging Neurosci* 11:27–27
77. Ni R, Rudin M, Klohs J (2018) Cortical hypoperfusion and reduced cerebral metabolic rate of oxygen in the arcAbeta mouse model of Alzheimer's disease. *Photoacoustics* 10:38–47
78. Ren W, et al (2019) Automated registration of magnetic resonance imaging and optoacoustic tomography data for experimental studies. *Neurophotonics* 6:1–10
79. Vaas M et al (2018) Vascular and tissue changes of magnetic susceptibility in the mouse brain after transient cerebral ischemia. *Transl Stroke Res* 9:426–435
80. Krämer SD et al (2018) Evaluation of (11)C-Me-NB1 as a potential PET radioligand for measuring GluN2B-containing NMDA receptors, drug occupancy, and receptor cross talk. *J Nucl Med* 59:698–703
81. Lin TN, He YY, Wu G, Khan M, Hsu CY (1993) Effect of brain edema on infarct volume in a focal cerebral ischemia model in rats. *Stroke* 24:117–121
82. Ma Y et al (2005) A three-dimensional digital atlas database of the adult C57BL/6J mouse brain by magnetic resonance microscopy. *Neuroscience* 135:1203–1215
83. Pettigrew LC et al (1996) Microtubular proteolysis in focal cerebral ischemia. *J Cereb Blood Flow Metab* 16:1189–1202
84. Dawson DA, Hallenbeck JM (1996) Acute focal ischemia-induced alterations in MAP2 immunostaining: description of temporal changes and utilization as a marker for volumetric assessment of acute brain injury. *J Cereb Blood Flow Metab* 16:170–174
85. Hosoya T et al (2017) In vivo TSPO and cannabinoid receptor type 2 availability early in post-stroke neuroinflammation in rats: a positron emission tomography study. *J Neuroinflamm* 14:69
86. Vandeputte C et al (2012) Small-animal PET imaging of the type 1 and type 2 cannabinoid receptors in a photothrombotic stroke model. *Eur J Nucl Med Mol Imag* 39:1796–1806
87. Jordan CJ, Xi Z-X (2019) Progress in brain cannabinoid CB(2) receptor research: from genes to behavior. *Neurosci Biobehav Rev* 98:208–220
88. Fernández-López D et al (2012) Reduced infarct size and accumulation of microglia in rats treated with WIN 55,212–2 after neonatal stroke. *Neuroscience* 207:307–315
89. Zhang M et al (2008) Modulation of the balance between cannabinoid CB(1) and CB(2) receptor activation during cerebral ischemic/reperfusion injury. *Neuroscience* 152:753–760
90. Govaerts SJ, Hermans E, Lambert DM (2004) Comparison of cannabinoid ligands affinities and efficacies in murine tissues and in transfected cells expressing human recombinant cannabinoid receptors. *Eur J Pharm Sci* 23:233–243
91. Yuan H et al (2013) Spatiotemporal uptake characteristics of [18]F-2-fluoro-2-deoxy-d-glucose in a Rat middle cerebral artery occlusion model. *Stroke* 44:2292–2299
92. Walberer M et al (2012) Potential of early [(18)F]-2-fluoro-2-deoxy-D-glucose positron emission tomography for identifying hypoperfusion and predicting fate of tissue in a rat embolic stroke model. *Stroke* 43:193–198
93. Jin T, Mehrens H, Wang P, Kim S-G (2017) Chemical exchange-sensitive spin-lock MRI of glucose analog 3-O-methyl- d -glucose in normal and ischemic brain. *J Cerebral Blood Flow Metab* 38: 0271678X1770741
94. Liu N-W, et al (2017) Evolutional characterization of photochemically induced stroke in rats: a multimodality imaging and molecular biological study. *Transl Stroke Res* 8
95. Backes H et al (2016) Glucose consumption of inflammatory cells masks metabolic deficits in the brain. *Neuroimage* 128:54–62
96. Sobrado M et al (2011) Longitudinal studies of ischemic penumbra by using 18F-FDG PET and MRI techniques in permanent and transient focal cerebral ischemia in rats. *Neuroimage* 57:45–54

Publisher's Note Springer Nature remains neutral with regard to jurisdictional claims in published maps and institutional affiliations.